

ULTRAVIOLET C II AND SI III TRANSIT SPECTROSCOPY AND MODELING OF THE EVAPORATING ATMOSPHERE OF GJ436b

R. O. PARKE LOYD¹, T. T. KOSKINEN², KEVIN FRANCE¹, CHRISTIAN SCHNEIDER³, SETH REDFIELD⁴

Draft version November 27, 2021

ABSTRACT

Hydrogen gas evaporating from the atmosphere of the hot-Neptune GJ436b absorbs over 50% of the stellar Ly α emission during transit. Given the planet’s atmospheric composition and energy-limited escape rate, this hydrogen outflow is expected to entrain heavier atoms such as C and O. We searched for C and Si in the escaping atmosphere of GJ436b using far-ultraviolet *HST* COS G130M observations made during the planet’s extended H I transit. These observations show no transit absorption in the C II 1334,1335 Å and Si III 1206 Å lines integrated over [-100, 100] km s⁻¹, imposing 95% (2σ) upper limits of 14% (C II) and 60% (Si III) depth on the transit of an opaque disk and 22% (C II) and 49% (Si III) depth on an extended, highly asymmetric transit similar to that of H I Ly α . C⁺ is likely present in the outflow according to a simulation we carried out using a spherically-symmetric, photochemical-hydrodynamical model. This simulation predicts a $\sim 2\%$ transit over the integrated bandpass, consistent with the data. At line center, we predict the C II transit depth to be as high as 19%. Our model predicts a neutral hydrogen escape rate of 1.6×10^9 g s⁻¹ (3.1×10^9 g s⁻¹ for all species) for an upper atmosphere composed of hydrogen and helium.

1. INTRODUCTION

The hot Neptune GJ436b was recently found to have an escaping atmosphere producing an extended transit that absorbs 56.3% of its host star’s Ly α (H I) emission (Kulow et al. 2014; Ehrenreich et al. 2015, hereafter E15; Bourrier et al. 2016, hereafter B16). This discovery classifies GJ436b as the only Neptune-mass planet among the three planets for which atmospheric escape has been observed in H I. The others, HD209458b (Vidal-Madjar et al. 2003) and HD189733b (Lecavelier Des Etangs et al. 2010) (note also a tentative detection for 55 Cnc b; Ehrenreich et al. 2012), have masses similar to Jupiter. For these two planets, atoms and ions more massive than H are also entrained in the escaping gas, specifically O I and C II, and Si III in the outflow of HD209458b (Vidal-Madjar et al. 2004; Linsky et al. 2010, though see also Ballester & Ben-Jaffel 2015 regarding Si III) and O I in the outflow of HD189733b (Ben-Jaffel & Ballester 2013). These species produce transit depths within a factor of two of the H I transits of those planets. The escape of heavier species implies that some combination of turbulence (eddy diffusion) and “drag” exerted on the heavier species by the escaping hydrogen must be at work (e.g. Vidal-Madjar et al. 2003, 2004; Koskinen et al. 2010).

This letter presents a search for transit absorption by C II, Si III, Si IV, and N V in the escaping atmosphere of GJ436b with the G130M grating of the Cosmic Origins Spectrograph (COS) onboard the *Hubble Space Telescope* (*HST*). We analyzed these data to place upper

limits on transit depths, examining simultaneous X-ray data from *Chandra* for information on stellar activity during transit. Further, we constructed an updated 1D hydrodynamic-photochemical model of GJ436b’s thermosphere that predicts H, He, C, and O escape from first principles and compared estimated transit depths with the data upper limits.

2. TRANSIT DATA AND ANALYSIS

2.1. *HST* Data

The MUSCLES Treasury Survey (France et al. 2016) recently obtained *HST* observations of GJ436. Scheduling constraints, including coordinated observations by X-ray observatories, precluded any effort to time the MUSCLES observations with a transit of the star’s hot Neptune. Nonetheless, three of five *HST* COS G130M exposures took place during the planet’s extended H I transit. The broadband visible-IR (i.e. not extended) transit occurred during the portion of *HST*’s orbit when Earth occulted the target, so it was not captured. We extracted lightcurves from the time-tagged photon lists provided for each exposure with an ~ 500 s cadence (adjusted to evenly divide each exposure) using the procedure outlined in Loyd & France (2014). In brief, this entailed counting weighted detector “events” in the appropriate regions of the spectrum and subtracting an estimate of background counts based on regions offset from the spectral signal trace. The event weights adjust for fixed pattern noise and detector dead time.

We created lightcurves for every strong line in the COS G130M bandpass that is not contaminated by geocoronal emission: C II 1334,1335 Å; Si III 1206 Å; Si IV 1393,1402 Å; and N V 1238,1242 Å. Si IV and N V are included for completeness, though absorption by these species is not expected due to their high formation temperatures. In creating lightcurves, we employed two separate velocity ranges over which we integrated emission line flux: The “blue integration”, [-100, 30] km s⁻¹, includes the veloc-

¹ Laboratory for Atmospheric and Space Physics, 600 UCB, Boulder, CO 80309, USA; robert.loyd@colorado.edu

² Lunar and Planetary Laboratory, University of Arizona, Tucson, AZ 85721, USA

³ European Space Research and Technology Centre (ESA/ESTEC), Keplerlaan 1, 2201 AZ Noordwijk, The Netherlands

⁴ Astronomy Department and Van Vleck Observatory, Wesleyan University, Middletown, CT 06459, USA

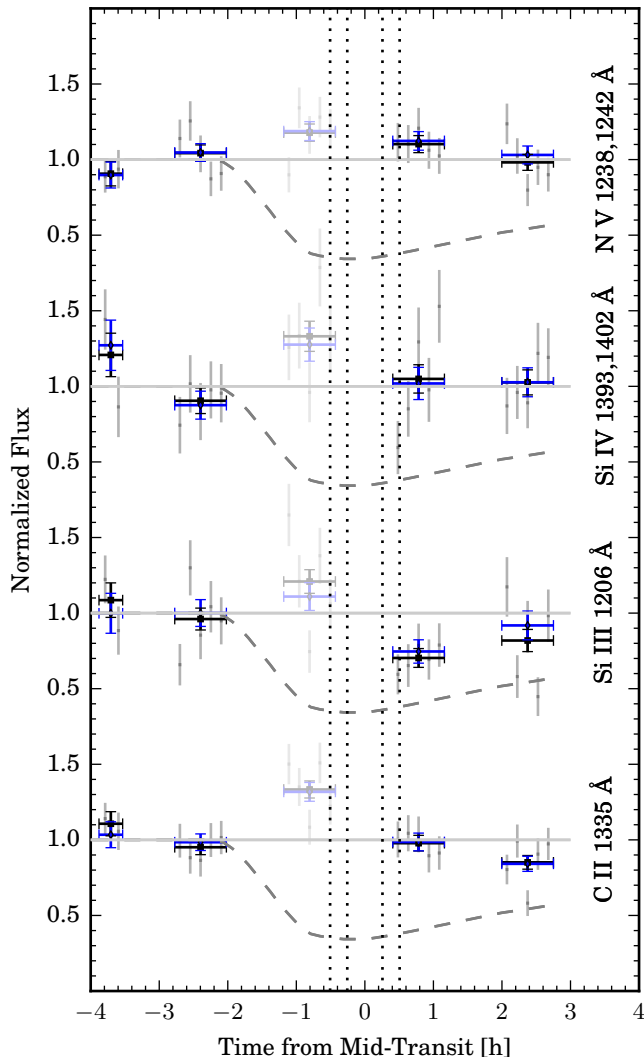


FIG. 1.— Lightcurves of line flux, normalized to the average flux from the first two exposures. Blue points represent flux integrated over $[-100, 30]$ km s^{-1} , black over $[-100, 100]$ km s^{-1} . Small points integrate flux over ~ 500 s intervals and large points integrate the full exposures, with horizontal bars showing the exposure duration. Dashed gray lines show the E15 H I transit model. Dotted vertical lines delimit the contact points of the broadband visible-IR transit. The third exposure is faint to emphasize that we discarded it from the analysis (Section 2.3).

ities predicted by the outflow model of E15, shifted to the heliocentric frame, and the “full integration”, $[-100, 100]$ km s^{-1} , includes all appreciable line flux.

Figure 1 displays the lightcurves, with the extended H I transit fit of E15 overplotted for comparison. Note that the same group has presented forward modeling with separate fits for each epoch of H I transit data in B16. We computed the transit phase of the observations using the ephemeris of Knutson et al. (2011). In addition to integrated time-series, we also searched for velocity-dependent absorption by comparing a spectrum coadded from the first two exposures (pre-transit) to one coadded from the last two exposures (extended H I transit; Figure 2).

2.1.1. Correction of a Systematic Wavelength Offset

Due to the instrument configuration, *HST* COS far-ultraviolet spectra have a small gap near their midpoint. To eliminate this gap, the MUSCLES survey observations employed two central wavelength (CENWAVE) settings, shifting from CENWAVE 1291 to 1318 between orbits 2 and 3. This spuriously shifted the measured wavelength of the lines for all 10 of the other MUSCLES targets. Left unaddressed, for these observations this shift produces an artificial transit signal at blueward wavelengths for C II and Si III. To correct for this effect, we applied wavelength offsets that produced the minimum χ^2 agreement between line profiles generated before and after the shift. These values are -9 (C II), -6 (Si III), 5 (Si IV), and -6 (N V) km s^{-1} .

The CENWAVE change did not significantly influence the measured line flux relative to the statistical noise. The absolute flux accuracy of the detector is estimated to be 5% (mainly due to fixed pattern noise; Debes et al. 2016). This is reduced to the 1% level when integrating a line.

2.2. Chandra Data

Data from the Chandra X-ray Observatory was obtained in tandem with the *HST* data, providing information on stellar activity. From this data, we created a light curve of the 300 – 2000 eV photon flux (Figure 3). The observation was performed with the ACIS-S detector on board *Chandra*. Source photons were extracted within a circle of radius 2 arcsec and we chose a large, nearby, source-free region to correct for the detector background.

2.3. Accounting for Activity-induced Variability

Limb brightening (Schlawin et al. 2010), stellar active regions (Llama & Shkolnik 2015), or any other spatial inhomogeneities in the stellar emission can modify the shape and overall depth of a transit curve. However, for GJ436b the depth and duration of the H I transit requires a cloud that covers a large fraction of the stellar disk, diluting effects on the transit from spatial inhomogeneities in stellar emission.

Temporal fluctuations in stellar emission on short timescales contribute to lightcurve scatter. These are constrained by two orbits of archival *HST* COS-G130M data (acquired ~ 14 h before transit and predating the present observations by about 2 years) to C II $3_{-2}^{+1}\%$, Si III $< 7\%$, and Si IV $< 6\%$ at the exposure timescale of ~ 45 min (Lloyd & France 2014; N V omitted in that work). We used these values to augment the lightcurve errors when exploring the parameter space of the transit models (Section 3).

We examined lightcurves for each line at high cadence and discovered a possible flare at ~ 700 s in the first exposure, visible in C II and Si III flux. Consequently, we excised the data from 650 – 800 s for all lines.

Stellar activity is also likely responsible for an enhancement in flux from all four lines throughout the third exposure. The simultaneity of these enhancements implies a common, physical source. One possible explanation is a flare, but this signal does not exhibit sharp, closely-aligned peaks in C II, Si III, and Si IV flux like flares observed on AD Leo and other M stars (Hawley et al. 2003; Lloyd & France 2014; France et al. 2016; Lloyd et al.

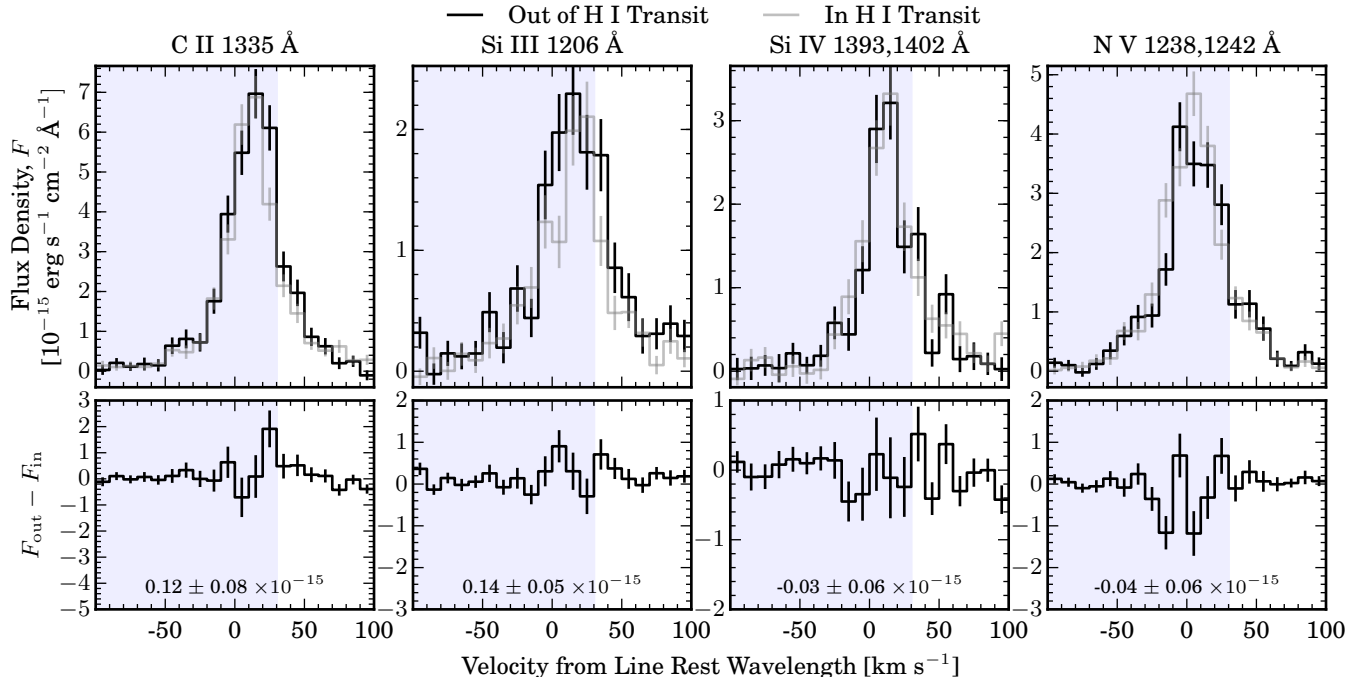


FIG. 2.— Comparison of line profiles prior to (first two exposures) and during the H I transit (final two exposures). Line wavelengths are listed above each panel, with multiple values indicating coadded lines. The spectra have been binned to 10 km s^{-1} per bin for display. The plotted wavelength range and the blue shaded area show the full and blue integration ranges used to create lightcurves. Numbers at the bottom of the lower plot give the flux difference of the full integrations.

2017 in prep). Those flares also show responses in Si III and Si IV many times greater than in N V, unlike this instance. No clear signal is seen in the stellar X-ray emission (Figure 3), though a slight enhancement peaking 1 – 2 h after the FUV lines might be present. Regardless of the origin, this signal could mask the beginning of a transit absorption signal, and because it cannot be accurately disentangled from superimposed transit absorption, we omitted it from further analysis.

We speculate that this activity enhancement could result from a star-planet interaction (SPI), such as an accretion stream from the planet. The N V flux, in particular, is well fit by a model wherein a hot-spot traverses the stellar disk at the sub-planetary point, but this fit is not significantly better than constant flux. In the full MUSCLES sample of stars, N V emission is strongly correlated with the ratio of planet mass to semi-major axis, suggesting N V might be a good tracer of SPIs (France et al. 2016). The hot spot hypothesis could be tested by additional *HST* G130M observations spanning a face-on view of the putative spot (near transit) through its disappearance behind the viewable stellar hemisphere (quadrature).

3. CONSTRAINTS ON TRANSIT SIGNALS

The lightcurves (Figure 1) and spectra (Figure 2) show no apparent transit signals. In order to derive upper limits, we explored the parameter space of two transit models that represent contrasting cases from the zoo of transit shapes that could arise from the many possible ion outflow geometries (e.g. tails, bow shocks, and accretion streams; Ness 1965; Matsakos et al. 2015; Cauley et al. 2015, 2016). As one model we chose the symmetric signal produced by an opaque disk transiting a uniformly illuminated stellar disk, representing scenarios where the

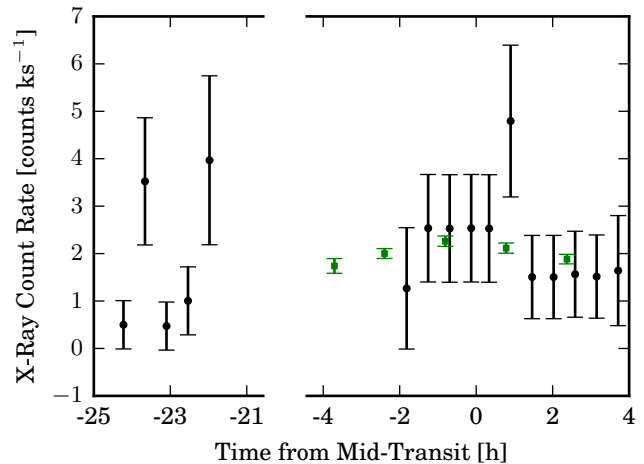


FIG. 3.— Lightcurve of the *Chandra* X-ray observations of GJ436, performed coincident with the *HST* observations. Green squares are the N V lightcurve normalized to 2 counts ks^{-1} , included for reference.

ions are decoupled from the H I outflow and symmetric about the projected planetary disk. At another extreme, we chose to scale the highly asymmetric H I Ly α transit curve of E15, representing scenarios where ions trail the planet in its orbit, as they would if they were coupled to the H I outflow.

The parameters of the opaque disk model are the baseline flux level and disk radius. To these we applied uniform priors for all positive values. While the data do not sample the transit of a disk equivalent to GJ436b’s broadband visible-IR radius very well (contact points shown as dotted lines in Figure 1), the geometry of the transit is such that the disk diameter is a substantial fraction of the path of the transit across the stellar disk. Conse-

TABLE 1
UPPER LIMIT ESTIMATES ON TRANSIT DEPTH.

Line	Occulting Disk		H-like	
	Blue ^a	Full ^b	Blue	Full
C II	<14%	<14%	<23%	<22%
Si III ^c	<58%	<60%	<44%	<49%
Si IV	<51%	<43%	<31%	<25%
N V	<13%	<12%	<10%	<10%

^a Based on blue integration ($[-100, 30]$ km s⁻¹) lightcurve. See Section 2.

^b Based on full integration ($[-100, 100]$ km s⁻¹) lightcurve.

quently, increases in transiting disk radius significantly increase transit duration as well as depth, causing the transit dip to overlap with exposure 4 and allowing that exposure to constrain the model. We account for the fact that the transit becomes grazing for radii $>1.8 R_p$.

The parameters of the H-like model are the baseline flux, ingress time (equivalently transit duration), and depth. We applied a uniform prior to all positive baseline flux values and all transit depths between zero and unity. For ingress time, we use a uniform prior that begins at the end of the first exposure to avoid hyper-extended transits that the data cannot constrain, and ends at the ingress of an equivalent opaque disk to avoid invoking contrived geometries for the absorbing cloud.

We used a Python implementation of the Markov-Chain Monte Carlo (MCMC) method, *emcee* (Foreman-Mackey et al. 2013), to sample the parameter space of these models. For all model and light curve combinations, no transit is detected. We report 95% (2σ) upper limits for each case in Table 1. A subset of the H-like models of particular interest consists of transits with duration fixed to that of the H I transit. We sampled this subset of models separately and found upper limits on H-like transit depth decreased by $\lesssim 2\%$.

The broad integration ranges we used could dilute transit absorption in narrow velocity ranges, so we searched all possible velocity ranges 5 – 100 km s⁻¹ in width for absorption. To assess the significance of the absorption signals this revealed, we applied the same methodology to 10^6 trials of data simulated assuming the null hypothesis of no true absorption, only white noise fluctuations. None of the absorption signals we found were sufficient to reject the null hypothesis at $> 2\sigma$ confidence.

4. MODEL THERMOSPHERE

4.1. Model Description

To interpret the upper limits on transit depth and place constraints on the mass loss rates, we simulated the thermosphere of GJ436b using an updated version of the 1D escape model of Koskinen et al. (2013a). This model solves the radial time-dependent equations of continuum, momentum, and energy simultaneously, with the ability to include several ion and neutral species. The model treats ionization, recombination, and basic photochemistry of H₂, H, He, C, O, H⁺, H₂⁺, H₃⁺, HeH⁺, C⁺, O⁺ and electrons. We excluded the related molecules H₂O, CO, and CH₄ and their chemistry, limiting C and O reactions to ionization, recombination, and charge exchange (excluding reactions with H₃⁺ that create molecular ions). The energy equation includes heating by the absorbed

stellar XUV radiation, heat conduction, adiabatic cooling and heating, vertical advection, viscous heating and radiative cooling by H₃⁺ infrared emission and H recombination. We included stellar gravity in our calculations to account for Roche lobe overflow effects along the substellar streamline, although these do not significantly affect mass loss from GJ436b. Magnetic fields are not considered. Though such fields would influence the flow of ions like C⁺, no measurements exist for exoplanetary magnetic fields.

The lower boundary conditions for the model are pressure, temperature, altitude, and composition. We adopted 1 μ bar as the lower boundary pressure. At this pressure level the T - P profile derived from secondary eclipse data (Line et al. 2014) gives a temperature of 583 K and an altitude of 3120 km. The lower boundary abundances of H₂, H, He, C and O are based on solar composition (Lodders 2003; see Section 4.3 for discussion) and a thermal equilibrium ratio of 0.032 for H/H₂.

We placed the upper boundary of the model at 10 R_p , well above the L1 point distance (5.8 R_p). The flow is collisional throughout the simulated range of altitudes, as verified using the Knudsen number. We impose linearly extrapolated upper boundary conditions on densities, velocity, and temperature that are valid above the Roche lobe and the sonic point. We ran the model with the stellar spectrum compiled by the MUSCLES survey (France et al. 2016; Youngblood et al. 2016; Loyd et al. 2016) with effective energies ranging from X-rays to the dissociation threshold of H₂ near 10 eV. This spectrum has an integrated EUV flux (100-911 Å) of 870 erg s⁻¹ cm⁻² at the 0.0308 AU semi-major axis of GJ436b (Lanotte et al. 2014).

4.2. Model Predictions for Outflow Rate, Composition, and Transit Depths

Our model predicts an escape rate of 1.6×10^9 g s⁻¹ for neutral hydrogen and 3.1×10^9 g s⁻¹ for all species. This exceeds the values of $10^8 - 10^9$ g s⁻¹ and $2.5 \pm 1 \times 10^8$ g s⁻¹ estimated by E15 and B16 from model fits to the H I transit data. Their lower escape rate estimates correspond to heating efficiencies below the 11% efficiency derived from our simulation. The escape estimate of the B16 model increases to a value agreeing with ours if they impose a fast stellar wind. However, B16 note that doing so produces a problematic fit to the transit data.

Figure 4 gives the temperature, outflow velocity, and composition profiles predicted by our model. The outflow velocity reaches 12 km s⁻¹ at the upper boundary, consistent with other simulations of escaping atmospheres (Murray-Clay et al. 2009). This value is below the 40 – 70 km s⁻¹ required by the B16 model to produce reasonable H I transit fits. B16 do not give the flow density at their lower boundary (near the Roche lobe), but Bourrier et al. (2015) quote a density of 0.4 cm⁻³ at 4 R_p when describing the precursor to the B16 model, a value that is significantly below our calculations (see Figure 4).

From the density profiles provided by the simulation, rough predictions of transit depth (at mid-transit) for a given line are possible. For altitudes sampled by the stellar disk at mid-transit but beyond the model boundary, we extrapolate the outflow density profile with an inverse square law. Alternatively, applying zero density or con-

stant density extrapolations produced roughly a factor of two difference in predicted transit depths. Beyond the planet’s Roche lobe ($\sim 5.8 R_p$), orbital dynamics, stellar winds, and radiation pressure influence the outflow, producing a broad and asymmetric absorption profile (see E15 and B16). To approximate modified flows, we explored a parameter space of broadened and shifted Voigt absorption profiles applied to our spherically-symmetric density profile.

Using this procedure to investigate H I Ly α absorption, we found that absorption profiles blueshifted by 20 – 40 km s $^{-1}$ and given a FWHM of 30 – 50 km s $^{-1}$ reproduced the $\sim 50\%$ absorption observed in the $[-120, -40]$ km s $^{-1}$ range by E15. For C II, FWHMs of 20 – 80 km s $^{-1}$ and no velocity shift yielded transit depths in the 1334.5 and 1335.7 Å lines of $\sim 2\%$, well below the data-imposed upper limits (Table 1). At the line centers, the C II transit depth could be as high as $\sim 19\%$ if the absorption is narrow (10 km s $^{-1}$). Unlike Ly α absorption, absorption at line center for ion lines like C II is not prevented by ISM absorption. This permits observations that probe lower levels of planetary outflows than Ly α , before the flow is accelerated to velocities outside the ISM absorption profile. However, neither the S/N nor the spectral resolution of the present data is sufficient to measure an $\sim 19\%$ transit over a band as narrow as 10 km s $^{-1}$.

An unexpected result of the model is the prediction of significant quantities of neutrals and H $_2$ in the outflow. H $_2$ at the predicted temperatures would have substantial populations in the $v = 1$ and 2 vibrational levels that have a dense forest of electronic transition lines in the FUV. This absorption could be measured against strong stellar emission lines, like Ly α , O VI 1032 Å, and C III 977 and 1175 Å by future missions with enhanced resolution and sensitivity in the FUV.

4.3. Limitations of the Model

The model’s omission of H $_2$ O, CO, and CH $_4$ could be important for GJ436b, as radiative cooling by these molecules could significantly reduce the mass loss heating efficiency of the atmosphere and thus lower the mass loss rate. This simplification was justified when applying the same model to hot Jupiters, such as HD209458b (Koskinen et al. 2013a), because detailed photochemical models predicted these molecules dissociate before reaching outflow altitudes (Moses et al. 2011; Lavvas et al. 2014), but this might not be the case for GJ436b (Moses et al. 2013). If substantial populations of these molecules are present, they could be transported into the thermosphere through turbulent mixing or collisional “drag” by rapidly escaping hydrogen, as we show in the following paragraphs.

Turbulent mixing can be parameterized in the form of an eddy diffusion coefficient, K_{zz} . We find that if $K_{zz} \gtrsim 10^8$ cm 2 s $^{-1}$, H $_2$ O can be transported above the 1 μ bar level. Estimates of K_{zz} for hot Jupiters (e.g. Moses et al. 2013) exceed this value. If similar values apply to GJ436b, then turbulence will transport molecules into the upper atmosphere.

Collisional drag can effectively transport any species

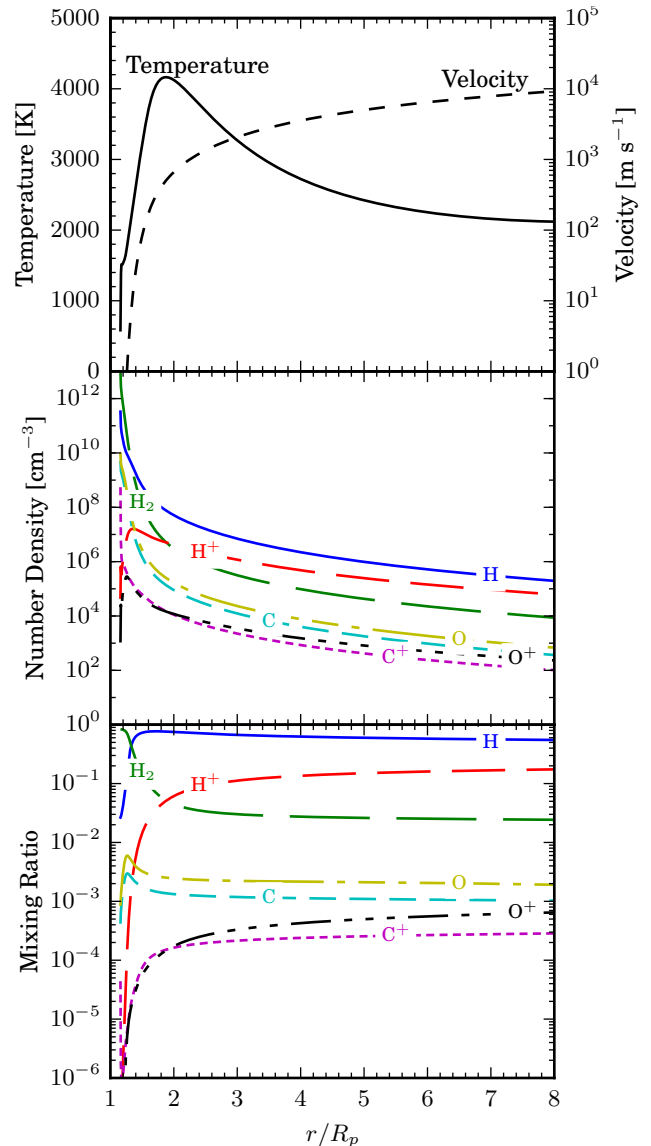


FIG. 4.— Outflow velocity, temperature, and composition of the model thermosphere as a function of height.

with a mass below the crossover mass,

$$m_{xo} = m_H + \frac{kT\dot{M}}{4\pi nDGM_p\mu}, \quad (1)$$

where the quantities involved are the mass of hydrogen, m_H ; Boltzmann constant, k ; gas temperature, T ; mass loss rate, \dot{M} ; coefficient of diffusion between the particle and hydrogen, nD ; gravitational constant, G ; planet mass M_p ; and mean molecular weight, μ (Hunten et al. 1987). Using the properties of the simulated outflow and the approximation

$$nD = 1.52 \times 10^{18} \sqrt{\frac{T}{\text{K}}} \left(\frac{1}{m_{xo}/\text{amu}} + 1 \right) \text{cm}^{-1}\text{s}^{-1} \quad (2)$$

(Koskinen et al. 2013b), we find a crossover mass of 28 amu, well above the mass of H $_2$ O and CH $_4$. Therefore, these molecules could be dragged along with the outflow.

The presence of molecules could be enhanced by super-

solar abundances of C and O. A super-solar metallicity is necessary to explain the ratio of $3.8 \mu\text{m}$ to $4.5 \mu\text{m}$ planetary emission measured via secondary eclipse (Stevenson et al. 2010; Madhusudhan & Seager 2011; Moses et al. 2013; Lanotte et al. 2014). However, for this work we assumed solar metallicity. The enhanced molecular cooling at higher metallicities could produce a shallower C II transit if it reduces the escape rate by an amount that overcomes the increased mixing ratio of C^+ , producing lower C^+ column densities at a given altitude.

The addition of H_2O , CO , and CH_4 to the model and the exploration of higher metallicities is beyond the scope of this Letter, but provides motivation for future work.

5. DISCUSSION AND CONCLUSIONS

We found no evidence of transit absorption by C II or Si III in *HST* COS G130M observations of GJ436b. The non-detection of a Si III transit is likely due to blockage of upward Si transport by condensation traps, namely clouds of forsterite (Mg_2SiO_4) and enstatite (MgSiO_3). These species have condensation curves (Fortney 2005) that cross the T - P profile for GJ436b retrieved by Line et al. (2014). Further, we estimate that Si bearing molecules are too heavy to be dragged into the upper atmosphere by escaping H. By these same arguments, Mg, another species observed in extended hot-Jupiter atmospheres (HD209458b and WASP-12b; Fossati et al. 2010; Vidal-Madjar et al. 2013; Bourrier et al. 2014, 2015), is unlikely to be present in the upper atmosphere of GJ436b.

The data impose upper limits on C II transit depth that are well below the H I $\text{Ly}\alpha$ transit, unlike the hot

Jupiter HD209458b (Vidal-Madjar et al. 2004; Linsky et al. 2010). To test this result, we employed a simulation of GJ436b's thermosphere to predict C II populations and found them significant, yet too low to produce sufficient transit absorption for detection with the present dataset: The data-imposed upper-limits of 14% (occulting disk transit) and 22% (H-like transit) substantially exceed the model-predicted transit depth of $\sim 2\%$. The simulation further predicted densities of H I capable of producing the $\gtrsim 50\%$ transit observed in previous data (E15) and an escape rate of $3.1 \times 10^9 \text{ g s}^{-1}$ (all species) that implies a mass loss efficiency of 11%.

The escape rate we estimated exceeds the $2.5 \pm 1 \times 10^8 \text{ g s}^{-1}$ estimate of B16. Further, the predicted densities and outflow velocities of these models differ significantly. Future work is needed to resolve the discrepancy between the Monte-Carlo forward modeling (“top-down”) approach of B16 and our photochemical-hydrodynamical (“bottom-up”) approach. A thorough understanding of escape from GJ436b is of particular importance given that it is currently the sole Neptune-mass planet with a known escaping atmosphere.

6. ACKNOWLEDGMENTS

The authors made use of Astropy code contributed by Stuart Little to compute barycentric light travel time corrections and are thankful for the large amount of effort this saved. The data presented here were obtained as part of the HST Guest Observing program #13650. This work was supported by NASA grants HST-GO-13650.01 to the University of Colorado at Boulder.

REFERENCES

- Ballester, G. E., & Ben-Jaffel, L. 2015, *ApJ*, 804, 116
 Ben-Jaffel, L., & Ballester, G. E. 2013, *A&A*, 553, A52
 Bourrier, V., Lecavelier des Etangs, A., Ehrenreich, D., Tanaka, Y. A., & Vidotto, A. A. 2016, *A&A*, 591, A121
 Bourrier, V., Lecavelier des Etangs, A., & Vidal-Madjar, A. 2014, *A&A*, 565, A105
 —. 2015, *A&A*, 573, A11
 Bourrier, V., Ehrenreich, D., & Lecavelier des Etangs, A. 2015, *A&A*, 582, A65
 Cauley, P. W., Redfield, S., Jensen, A. G., & Barman, T. 2016, *AJ*, 152, 20
 Cauley, P. W., Redfield, S., Jensen, A. G., et al. 2015, *ApJ*, 810, 13
 Debes, J., et al. 2016, *STScI*
 Ehrenreich, D., Bourrier, V., Bonfils, X., et al. 2012, *A&A*, 547, A18
 Ehrenreich, D., Bourrier, V., Wheatley, P. J., et al. 2015, *Nature*, 522, 459
 Foreman-Mackey, D., Hogg, D. W., Lang, D., & Goodman, J. 2013, *PASP*, 125, 306
 Fortney, J. J. 2005, *MNRAS*, 364, 649
 Fossati, L., Haswell, C. A., Froning, C. S., et al. 2010, *ApJ*, 714, L222
 France, K., Loyd, R. O. P., Youngblood, A., et al. 2016, *ApJ*, 820, 89
 Hawley, S. L., Allred, J. C., Johns-Krull, C. M., et al. 2003, *ApJ*, 597, 535
 Hunten, D. M., Pepin, R. O., & Walker, J. C. G. 1987, *Icarus*, 69, 532
 Knutson, H. A., Madhusudhan, N., Cowan, N. B., et al. 2011, *ApJ*, 735, 27
 Koskinen, T. T., Harris, M. J., Yelle, R. V., & Lavvas, P. 2013a, *Icarus*, 226, 1678
 Koskinen, T. T., Yelle, R. V., Harris, M. J., & Lavvas, P. 2013b, *Icarus*, 226, 1695
 Koskinen, T. T., Yelle, R. V., Lavvas, P., & Lewis, N. K. 2010, *ApJ*, 723, 116
 Kulow, J. R., France, K., Linsky, J., & Loyd, R. O. P. 2014, *ApJ*, 786, 132
 Lanotte, A. A., Gillon, M., Demory, B.-O., et al. 2014, *A&A*, 572, A73
 Lavvas, P., Koskinen, T., & Yelle, R. V. 2014, *ApJ*, 796, 15
 Lecavelier Des Etangs, A., Ehrenreich, D., Vidal-Madjar, A., et al. 2010, *A&A*, 514, A72
 Line, M. R., Knutson, H., Wolf, A. S., & Yung, Y. L. 2014, *ApJ*, 783, 70
 Linsky, J. L., Yang, H., France, K., et al. 2010, *ApJ*, 717, 1291
 Llama, J., & Shkolnik, E. L. 2015, *ApJ*, 802, 41
 Lodders, K. 2003, *ApJ*, 591, 1220
 Loyd, R. O. P., & France, K. 2014, *ApJS*, 211, 9
 Loyd, R. O. P., France, K., Youngblood, A., et al. 2016, *ApJ*, 824, 102
 Loyd, R. O. P., et al. 2017, *ApJ* in prep.
 Madhusudhan, N., & Seager, S. 2011, *ApJ*, 729, 41
 Matsakos, T., Uribe, A., & Königl, A. 2015, *A&A*, 578, A6
 Moses, J. I., Visscher, C., Fortney, J. J., et al. 2011, *ApJ*, 737, 15
 Moses, J. I., Line, M. R., Visscher, C., et al. 2013, *ApJ*, 777, 34
 Murray-Clay, R. A., Chiang, E. I., & Murray, N. 2009, *ApJ*, 693, 23
 Ness, N. F. 1965, *J. Geophys. Res.*, 70, 2989
 Schlawin, E., Agol, E., Walkowicz, L. M., Covey, K., & Lloyd, J. P. 2010, *ApJ*, 722, L75
 Stevenson, K. B., Harrington, J., Nymeyer, S., et al. 2010, *Nature*, 464, 1161
 Vidal-Madjar, A., Lecavelier des Etangs, A., Désert, J.-M., et al. 2003, *Nature*, 422, 143
 Vidal-Madjar, A., Désert, J.-M., Lecavelier des Etangs, A., et al. 2004, *ApJ*, 604, L69
 Vidal-Madjar, A., Huitson, C. M., Bourrier, V., et al. 2013, *A&A*, 560, A54

Youngblood, A., France, K., Parke Loyd, R. O., et al. 2016, ApJ, 824, 101